Characteristic Frequencies of Transonic Diffuser Flow Oscillations

T. J. Bogar,* M. Sajben,† and J. C. Kroutil‡
McDonnell Douglas Corporation, St. Louis, Missouri

The time-mean and unsteady flow characteristics of a supercritical transonic diffuser are investigated as a function of shock Mach number and diffuser length. The flow is either attached or undergoes shock-induced separation, depending on shock strength. The power spectral density distributions of the unsteady shock motion display up to three distinct peaks, depending on flow conditions. For attached flow, the characteristic frequencies scale with the distance from the shock to the diffuser exhaust. Their origin is acoustic and frequencies up to the third harmonic are observed. For shock-induced separation, the single characteristic frequency observed does not follow acoustic predictions. The mechanism of these oscillations may be related to the core flow dimensions or to the spectral amplitude response characteristics of the terminal shock.

Nomenclature

a = velocity of sound
C = shock/wall pressure cross correlation
C_f = skin friction coefficient
f = frequency
h = channel height
k = wave number in fluid at rest
L = streamwise length (between points indicated by dual subscripts)
M = Mach number
p = pressure
q = dynamic pressure ($\frac{1}{2}\rho u^2$)
S = power spectral density
t = time
T = propagation time
u = streamwise velocity component
x = streamwise coordinate ($x=0$ at throat, positive streamwise)
y = vertical coordinate ($y=0$ on lower wall, positive upward)
δ^* = displacement thickness
θ = momentum thickness
ϕ = phase shift
ν_e = pressure ratio (p_{to}/p_{se})
ρ = density
τ = time delay
ω = angular frequency

Subscripts

c = end of core flow
d = separation (detachment) point
e = exit station
i = inlet station
ℓ = lower wall ($y=0$)
m = midstream ($y=0.432$, core probe and line-scan system scanning height)
o = plenum
r = reattachment point
s = static
t = total
u = upper wall [$y=h(x)$]
v = exhaust (vent) to laboratory
σ = on surface of shock
$(\ )_*$ = throat
$+(-)$ = downstream (upstream) moving wave

Superscripts

$(\bar{\ })$ = time-mean component
$(\ )'$ = time-dependent component
$(\hat{\ })$ = rms of time-dependent component
$(\tilde{\ })$ = normalized by throat height (h_*)

Introduction

THIS paper presents results of the latest study in an experimental program[1-4] to investigate nominally two-dimensional transonic flows in convergent/divergent channels with a sonic throat and a moderately strong normal shock downstream of the throat. The investigations include the determination of time-mean flowfield properties and a detailed study of the unsteady aspects of the flow, with particular attention to the coherent, low-frequency natural fluctuations observed under virtually all operating conditions. The program is intended to support development of numerical flowfield prediction methods for supersonic inlets of turbojets and ramjets.[5-8]

The configurations investigated in this series (Fig. 1) are two-dimensional idealizations of inlet flowfields. With glass sidewalls, access is provided for optical diagnostic methods capable of yielding information not obtainable from models that more closely duplicate operational inlets. The convergent/divergent diffuser configuration models those portions of supercritical inlet flows that pose the most difficult prediction problems. Most importantly, the flow contains a normal shock/turbulent boundary-layer interaction (SBLI) region combined with a subsonic, adverse pressure gradient region behind the shock. This pattern is generally present in both supercritical and subcritical inlets, in transonic airfoil flows,[9,10] and in transonic compressor rotor passages.[11] The dynamic aspects of the interaction are manifested in practice as dynamic distortion in inlets, pressure oscillations in ramjets,[12] and airfoil, wing, and control-surface buffet in external flows,[13] and may play a role in certain types of transonic compressor stalls.

Earlier studies in this program dealt with several diffuser configurations having exit-to-throat area ratios of 1.84-2.5,

---

Presented as Paper 81-1291 at the AIAA 14th Fluid and Plasma Dynamics Conference, Palo Alto, Calif., June 23-25, 1981; submitted June 14, 1982; revision received Nov. 19, 1982. Copyright © American Institute of Aeronautics and Astronautics, Inc., 1982. All rights reserved.

*Scientist, McDonnell Douglas Research Laboratories. Senior Member AIAA.

†Principal Scientist, McDonnell Douglas Research Laboratories. Associate Fellow AIAA.

‡Unit Chief, McDonnell Douglas Research Laboratories. Member AIAA.

(a) No separation (NS)
$M_{\sigma u} < 1.27$; $A_e/A_* \lesssim 1.6$

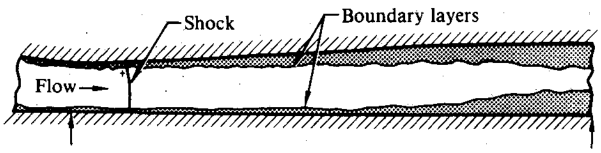

(b) Pressure-gradient-induced separation (PGIS)
$M_{\sigma u} < 1.27$, $A_e/A_* \gtrsim 1.6$

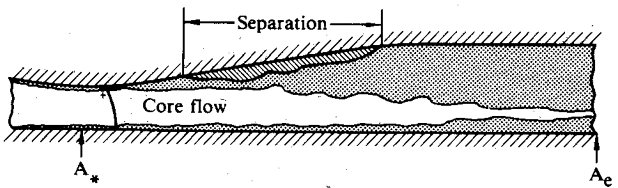

(c) Shock-induced separation (SIS)
$M_{\sigma u} > 1.3$

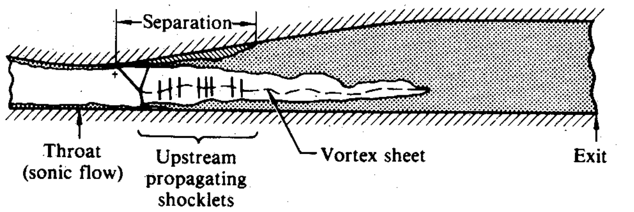

Fig. 1 Supercritical diffuser flow patterns ($M_{\sigma u}$ is the local Mach number at + signs).

Side view

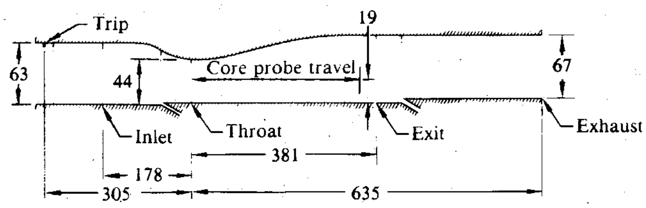

Top view

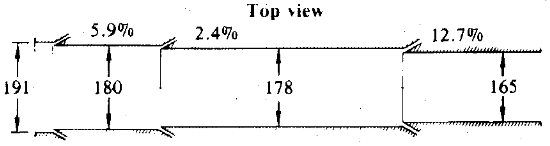

Dimensions in millimeters
Vertical scale doubled
Slot sizes enlarged for clarity
Percentages denote area decrease at slots

Fig. 2 Layout of the diffuser model.

whereas the present study deals with a diffuser having an area ratio of 1.5.

The flow patterns found in this program consistently belonged to one of the three types shown in Fig. 1, depending on the Mach number immediately before the normal shock ($M_{\sigma u}$) and on the area ratio. In the present experiment, attached flow (Fig. 1a) was found for shock Mach numbers below 1.27. This pattern will be referred to as not separated (NS). All earlier models displayed a pressure-gradient-induced separation (PGIS, Fig. 1b) below $M_{\sigma u} \cong 1.3$. If the shock Mach number exceeds these limiting values, shock-induced separation (SIS, Fig. 1c) occurs in all cases. Alternately, the flows can also be described as strong or weak shock cases, depending on the presence or absence of SIS. The maximum shock Mach number explored was 1.4 and the top wall boundary layer at the throat was turbulent in all cases.

This paper describes the experimental and diagnostic equipment, the time-mean flow properties, and the naturally occurring fluctuations. Particular emphasis is placed on determining the characteristic (natural) frequencies associated with those oscillations that are coherent along the entire diffuser length. The effect of the geometric channel length was investigated by varying the length of the channel containing subsonic flow over a 2:1 range.

Two related papers[14,15] investigate the diffuser model described here under the influence of periodic perturbations imposed at the downstream end of the diffuser.

Table 1 Constants for channel height calculation

Constant	Converging	Diverging
α	1.4114	1.5
$\tilde{\ell}$	−2.598	7.216
C_1	0.81	2.25
C_2	1.0	0
C_3	0.5	—
C_4	0.6	0.6

Experimental Equipment and Procedures

Diffuser Model

The diffuser model (Fig. 2) is a convergent/divergent channel with a flat bottom and a contoured top wall defined by

$$\tilde{h}(\tilde{x}) = \frac{\alpha \cosh\zeta}{(\alpha - 1) + \cosh\zeta} \tag{1}$$

where

$$\zeta = \frac{C_1 (\tilde{x}/\tilde{\ell})\,[1 + C_2 (\tilde{x}/\tilde{\ell})\,]^{C_3}}{(1 - \tilde{x}/\tilde{\ell})^{C_4}} \tag{2}$$

Values for the various constants are given in Table 1 for both the converging and diverging sections of the channel.

An arbitrarily selected location within the constant-area section upstream of the throat ($\tilde{x}_i = -4.04$) is designated as a nominal inlet station. The nominal exit station is at $\tilde{x}_e = 8.65$, within the constant-area section downstream of the divergent portion.

Side and bottom wall boundary-layer growth is limited by three sets of forward-facing (ram) suction slots. The percentages given in Fig. 2 are nearly equal to the fraction of mass flow removed at each slot; the flow is choked at the two upstream slots and nearly choked at the third slot. The side walls of the model are fitted with 2.54 cm thick, schlieren-quality glass panels.

Dry, filtered, metered air is supplied to the model from a 51 cm diam plenum chamber immediately upstream. The plenum is well screened and has a smoothly contoured transition to the model with a contraction ratio of 17:1, providing highly uniform, low-turbulence flow. A spanwise insert extending 0.51 mm into the flow trips the top wall boundary layer at $\tilde{x} = -6.92$. The flow from the model is vented to the atmosphere, providing a constant-pressure downstream boundary condition. Plenum chamber pressure ranged up to 35 kPa, and mass flow rates at the plenum chamber exit ranged up to 2.2 kg/s. Supply air temperature variations varied the Reynolds number at 6.4-8.4 × 10^5, based on throat height and throat conditions.

The downstream end of the model could be fitted with constant-area extensions, which allowed the model length (from throat to exhaust) to be increased from 14.4 to 30.5 throat heights in increments of approximately 1 throat height.

The top and bottom walls of the model contain over 100 orifices for measuring the time-mean wall static-pressure distribution. Seven ports are located along the top wall to accommodate sensors for fluctuating surface pressures. Two similar ports are also located on the bottom wall at the exit station. The inlet and exit stations of the model also each contain six ports, three on the top wall and one each on the other three sides, for boundary-layer probes.

Instrumentation

Miniature, fast-response transducers were flush mounted at nine ports to measure unsteady surface pressures.

A line-scan television-type camera together with a shadowgraph optical system[16,17] was used to measure the time-dependent shock location. The camera has a spatial resolution of 0.3 mm and a scanning rate of 4 kHz.

A dual-pressure probe incorporating two transducers was used to measure the instantaneous total and static pressures in the core flow. The probe, mounted on a traversing drive imbedded in the removable bottom wall of the model, could be continuously positioned in the streamwise direction at $\tilde{x} = 0$-8 at a height of 19 mm above the bottom wall. The line-scan camera was also focused at this height. When in place, the probe caused no discernible alteration in measured flow properties. Separate calibration indicated no transonic or interference effects for the range of Mach numbers encountered in the core flow.

Oil flow traces using a solution of oil and lampblack were used to detect the direction of the time-mean skin friction.

The boundary layers at the inlet and exit stations of the model were measured with a miniature total-pressure probe constructed from a length of stainless steel tubing formed into a hook shape. The end of the tube was flattened so that the orifice was nearly rectangular with dimensions of 0.294 mm parallel to the wall and 0.0254 mm perpendicular to the wall.

A vertical rake of eleven 0.8 mm diam total-pressure tubes was used to measure the total pressure distribution at the exit station. A long, slender sting tipped with a fast-response pressure transducer was used to measure the mean and fluctuating total-pressure profiles along the plane of symmetry of the channel.

High-speed (5000 frames/s) schlieren motion pictures were made of the flowfield, with the field of view extending from $\tilde{x} = -1$ to $+8$.

Data Acquisition and Processing

Twenty channels of steady data were routinely recorded, including operational variables such as plenum chamber pressure, suction pressures, temperatures and rms values of time-dependent quantities such as shock position and selected surface pressures. All unsteady data were amplified, low-pass filtered at 10 kHz, and recorded on FM tape. The FM tapes were replayed into a 400-point spectrum analyzing system to obtain power spectral density distributions and cross correlations.

Flow Characteristics

Test Parameters

Two parameters were used to define a particular test condition, $M_{\sigma u}$ and $L_{\sigma v}$. $M_{\sigma u}$ is the local Mach number at the edge of the top wall boundary layer immediately upstream of the shock, and $L_{\sigma v}$ is the distance from the shock to the model exhaust. $M_{\sigma u}$ and the mean location of the shock along the top wall $x_{\sigma u}$ were determined from top wall mean static-pressure distributions, several of which are displayed in Fig. 3. The minimum pressure defines the shock location, and $M_{\sigma u}$ is determined from the ratio of the minimum static pressure and the inlet total pressure. $M_{\sigma u}$ determines the pressure jump imposed by the shock on the boundary layer and is an appropriate variable to characterize the shock/boundary-layer interactions.

Figure 3 also contains distributions of the local dynamic pressure q (normalized by p_{to}) for three cases. The dynamic pressure was calculated on the basis of the mean top wall static pressures and the mean total pressures measured by the core flow probe.

Inlet/Exit Boundary Conditions

The top wall boundary layer was tripped at $\tilde{x} = -6.92$. The bottom and side wall boundary layers were initiated at the sharp downstream edges of ram-type suction slots shortly before the throat. Since the Reynolds number based on distance from the sharp leading edge and conditions before the shock was always less than 3.4×10^6 and strong, favorable

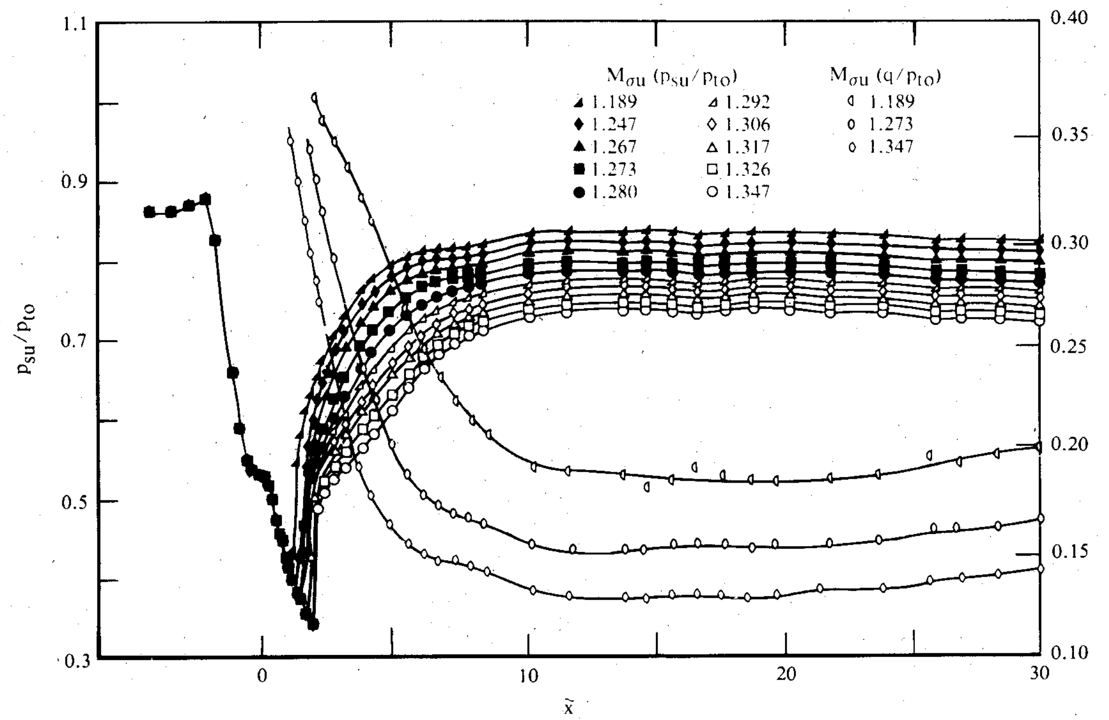

Fig. 3 Top wall pressure distributions and core flow dynamic pressures.

Table 2 Top wall boundary-layer properties

M_{ou}	1.159	1.235	1.269	1.353
Inlet[a]				
$\tilde{\delta}^*$	0.0151	0.0167	0.0170	0.0163
	0.0159			0.0161
	0.0167			0.0166
$\tilde{\theta}$	0.0097	0.0105	0.0108	0.0103
	0.0111			0.0111
	0.0111			0.0109
$C_f \times 10^3$	3.34	3.32	3.27	3.24
	3.21			3.07
	3.34			3.22
Throat				
$\tilde{\delta}^*$	0.00645	0.00651	0.00661	0.00651
$\tilde{\theta}$	0.00342	0.00346	0.00352	0.00347
$C_f \times 10^3$	3.01	3.00	2.98	2.95
Exit[a]				
$\tilde{\delta}^*$	0.1052	0.1111	0.1768	0.3461
	0.1196			0.3188
	0.1120			0.2660
$\tilde{\theta}$	0.0663	0.0704	0.1043	0.1497
	0.0684			0.1528
	0.0727			0.1175
$C_f \times 10^3$	1.60	1.64	1.31	0.37
	1.28			0.54
	1.45			0.55

[a] The three entries per quantity denote results from measurements made at model centerline and 41 mm lef and right (facing downstream) of centerline, respectively.

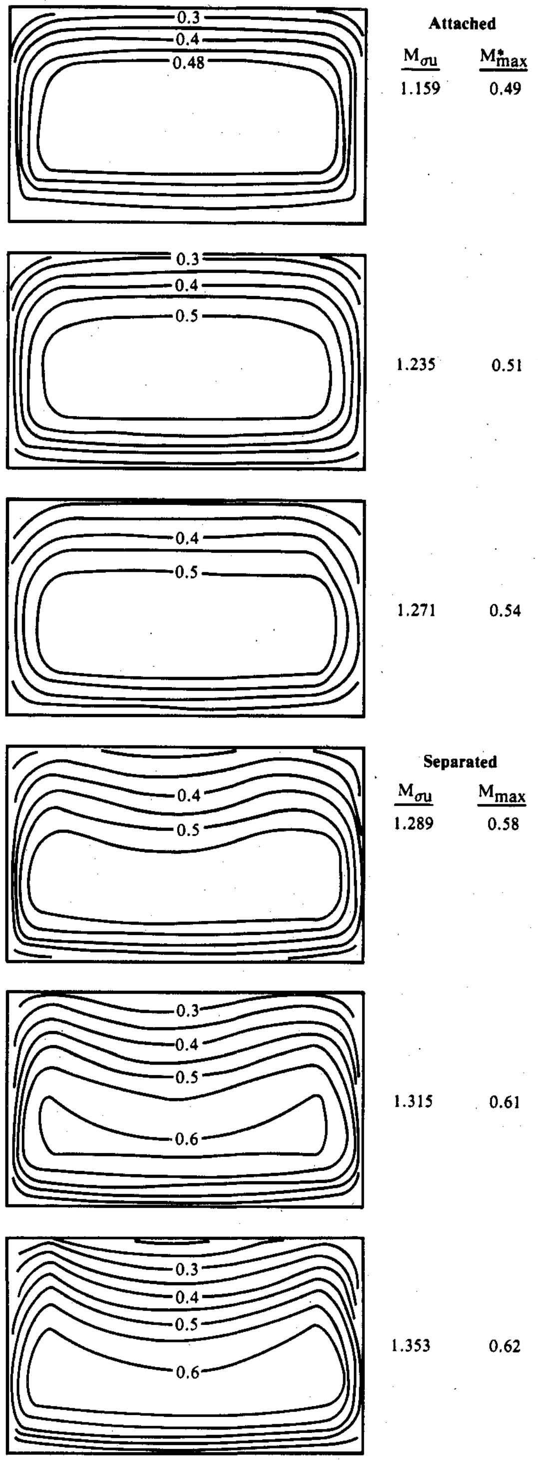

*Highest value Mach number attained in exit plane.

Fig. 4 Mach number contours at exit station.

pressure gradients were present, the side and bottom wall boundary layers were expected to remain laminar up to the shock.

Boundary-layer measurements were made with the miniature total-pressure probe on the top wall at the inlet and exit stations, both on and 41 mm to either side of the model centerline. The measured velocity profiles clearly indicate that the top wall boundary layers are turbulent. The measured values of displacement thickness, momentum thickness, and skin friction coefficient are presented in Table 2. The values of the boundary-layer parameters at the throat were calculated from the inlet centerline values and measured pressure distributions by an integral momentum scheme.[18] The boundary layer at the inlet is highly two-dimensional for all Mach numbers. The degree of two-dimensionality at the exit is illustrated in more detail by the Mach number contours (Fig. 4) based on measurements at 17 spanwise positions at the exit station using the 11-prong total-pressure rake. Mach numbers were calculated using the time-mean top wall static pressure. The contour plots show excellent two-dimensionality in attached flows ($M_{ou} < 1.27$) and a characteristic thickening of the top wall boundary layer at the centerline in separated flows. Oil flow traces on the top wall indicate the presence of secondary flows directed inward near the reattachment point, causing the influx of low-speed fluid from the sides and the increased thickness of the boundary layer near the center.

Shock and Separation Bubble Features

Oil flow traces were used to determine the extent of the separation bubble (Fig. 5). These studies showed no evidence of flow separation on the bottom wall at any test condition and none on the top wall for weak shocks. A separation bubble first appears on the top wall at $M_{ou} \approx 1.27$ and quickly enlarges to cover four throat heights in length.

Spark schlieren photographs (Fig. 6) reveal differences between the subsonic boundary-layer structures found in the weak and strong shock cases. For weak shocks, both layers are attached and relatively thin, and an inviscid region of constant mean total pressure (the core flow) continues past the end of the unextended channel. For strong shocks, the top wall layer separates and thickens extremely rapidly, several times faster than that observed with weak shocks. The top and bottom boundary layers merge well inside the unextended diffuser.

Streamwise Distribution

The nondimensionalized top wall surface pressure distributions (Fig. 3) were not altered by the addition of duct extension segments further downstream, as long as ν_e was

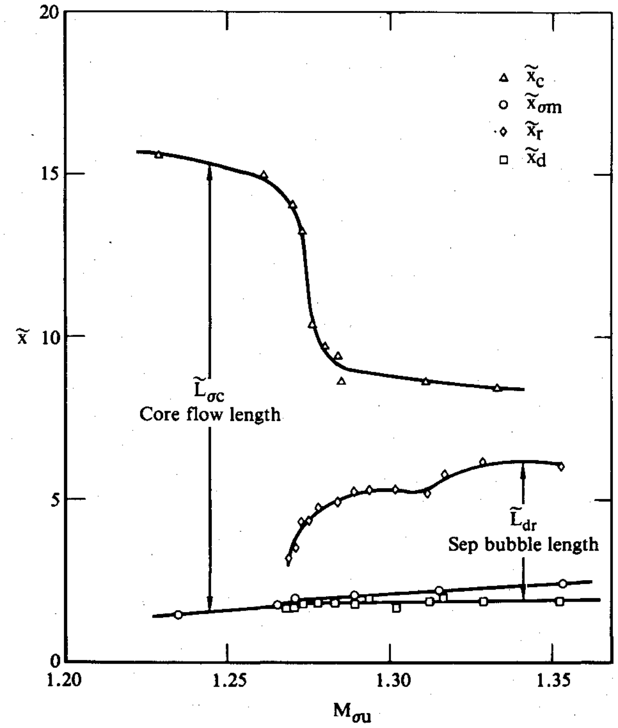

Fig. 5 Core flow and separation bubble lengths.

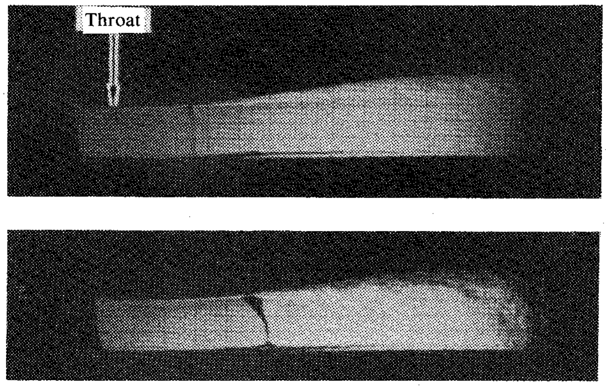

Fig. 6 Spark schlieren photographs of attached and separated flow at $M_{\sigma u} = 1.235$ (top) and 1.353 (bottom). Grid spacing is 25.4 mm horizontally, 12.7 mm vertically.

kept constant. For attached flows the distributions are smooth, the recovery reaching a maximum near $\tilde{x} \approx 12$. Beyond this location, the pressure decreases slightly to balance wall friction in the constant-area portion of the duct.

The length of the time-mean core flow region was determined by measuring the vertical, time-mean total pressure profiles in the plane of symmetry at various streamwise locations. The region was defined as that within which the mean total pressure is between 98 and 100% of the time-mean, postshock total pressure at $y = y_m$. The length $L_{\sigma c}$ is the streamwise distance between the time-mean, midstream shock locations $\tilde{x}_{\sigma m}$ and the downstream-most point of the (approximately triangular) region. The results are shown in Fig. 5. The dramatic reduction in core flow length at $M_{\sigma u} \approx 1.27$ results from the rapid boundary-layer growth associated with SIS.

The onset of SIS causes significant changes in the character of most time-mean flow properties. These changes may be useful in diagnosing the onset of SIS when separation cannot be detected directly. The ranges over which the NS/SIS transition occurs are illustrated in Fig. 7 for three time-mean quantities.

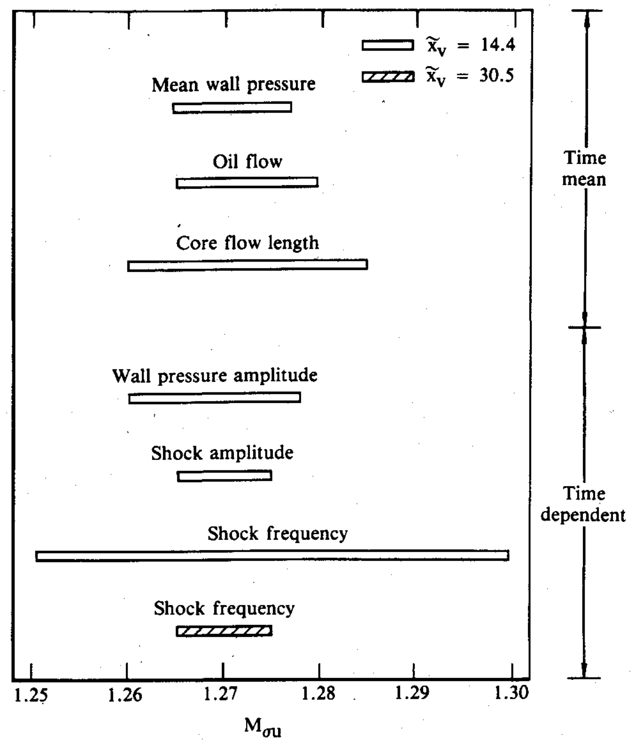

Fig. 7 Mach number range of transition, as determined by various measured quantities.

Unsteady Flow Characteristics

A detailed survey was made of the static wall pressures at seven streamwise locations, the static and total pressures in the core flow, and the shock displacement as a function of $M_{\sigma u}$ for the unextended channel.

Pressure Measurements

Figure 8 displays the top wall static-pressure fluctuation (rms) intensities, normalized with the local $q(x)$, as a function of $M_{\sigma u}$. The most striking feature of the curves is a dramatic change in the vicinity of $M_{\sigma u} = 1.27$ associated with the onset of SIS. The three measurement stations nearest the shock show an almost discontinuous change in magnitude as separation occurs. A sharp increase in the fluctuations at $\tilde{x} = 2.43$ begins as low as $M_{\sigma u} = 1.25$; its origin is described below.

The shadowgraph flow image reveals that the transition from fully NS to fully SIS occurs intermittently at frequencies between 0.5 and 3 Hz, manifested by the intermittent, rapid thickening of the top wall boundary layer. The transition is also detectable in the wall pressure signals immediately downstream of the shock. Although most prevalent at $M_{\sigma u} = 1.275$, the transition is visible in the shadowgraph image down to $M_{\sigma u} = 1.262$, which corresponds to the Mach number at which the oil flow data (Fig. 5) indicate the appearance of the separation bubble. The oil flow indicates only the time-mean skin friction and cannot establish whether the flow is fully or only intermittently separated.

The intermittence of separation is related to the fluctuating strength of the shock. The shock may not be strong enough, in the mean, to induce separation, but it can momentarily acquire the required strength. This intermittent transition can account for the steep increase in the wall pressure fluctuations at $\tilde{x} = 2.43$, preceding the discontinuous jump when the flow becomes fully separated.

Shock Displacement Measurements

Figure 8 also shows the normalized shock-fluctuation magnitude as a function of $M_{\sigma u}$ for all $L_{\sigma v}$ values. The shape of the curve is similar to that of the wall pressure (Fig. 8,

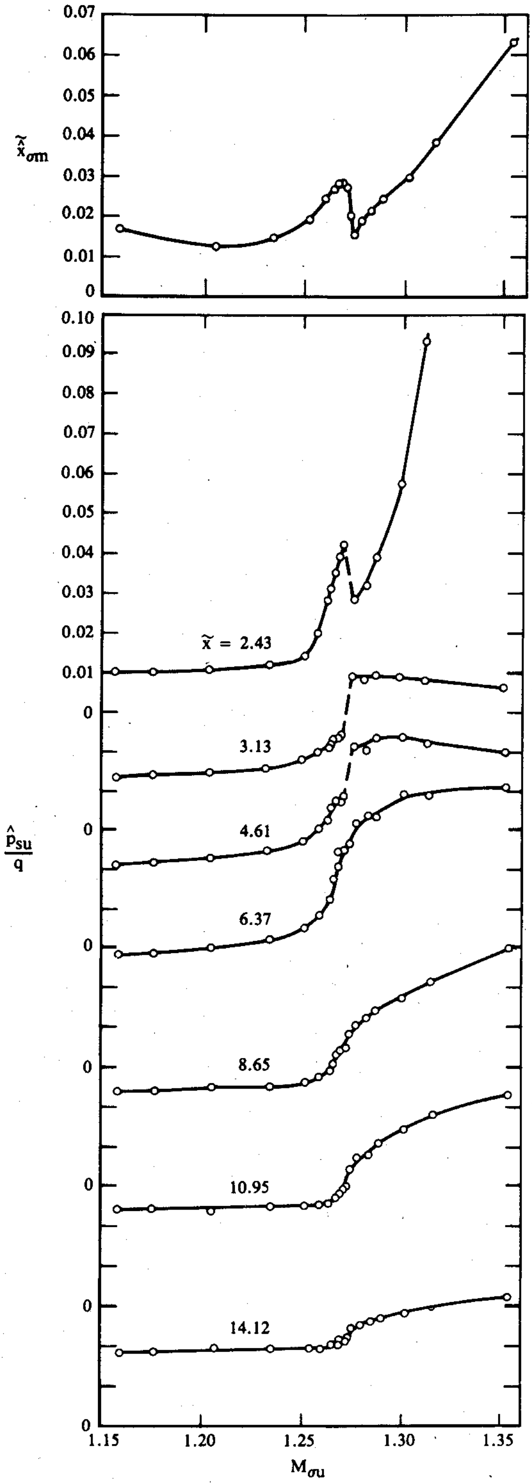

Fig. 8 Unsteady shock motion and top wall pressure amplitudes.

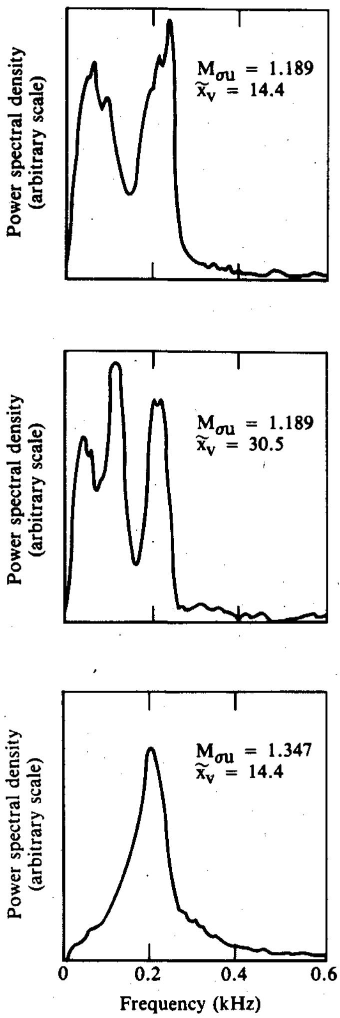

Fig. 9 Shock motion power spectral density distributions.

$\tilde{x}=2.43$). The highest value achieved, however, is only slightly more than 6% of the throat height, compared with the >40% of the throat height observed in the previous model.[4] In the previous model, the pressure fluctuations associated with local boundary-layer turbulence at the duct end contained much of their energy at frequencies near the shock frequencies. This situation does not occur here, probably accounting for the lower shock amplitudes.

Shock displacement power spectral density distributions (PSD) show well-defined, low-frequency peaks (Fig. 9). The number and frequencies of these peaks are strong functions of both $M_{\sigma u}$ and x_v: two or three exist in the NS mode and only one in the SIS mode. Figure 10 shows plots of the natural frequencies for the unextended and the fully extended channel.

The NS/SIS transition causes marked changes over a narrow $M_{\sigma u}$ range in various unsteady properties. As shown in Fig. 7, the transitional ranges based on dynamic variables overlap the range based on time-mean properties. Top wall transition is determined to occur at $M_{\sigma u}=1.27\pm0.02$.

Natural Frequencies

Weak Shocks

For attached flows, the natural frequencies were found to vary inversely with the channel length, suggesting the possibility that the natural frequencies are associated with the longitudinal acoustic modes of the channel.

Longitudinal acoustic oscillations in slender channels can be modeled by an inviscid, linearized, quasi-one-dimensional theory, taking into account the streamwise variation of mean velocity and pressure. The open downstream end is represented by the conventional constant-pressure boundary condition. The reflective properties of the normal shock were determined by Culick[19] in terms of a complex reflection coefficient specifying the amplitude and phase of the reflected wave. For the conditions of the present experiment, the calculated reflection coefficient amplitude is always <0.08, i.e., the shock reflects weakly.

It is relatively easy to predict the frequencies at which the given boundary conditions can be satisfied. The procedure of the Appendix yields:

$$f_n=\left[\frac{2n-1}{4}-\frac{\phi}{4\pi}\right]\Big/\int_{x_\sigma}^{x_v}\frac{\mathrm{d}x}{a(x)\left[1-M^2(x)\right]},\quad n=1,2,3,\ldots \tag{3}$$

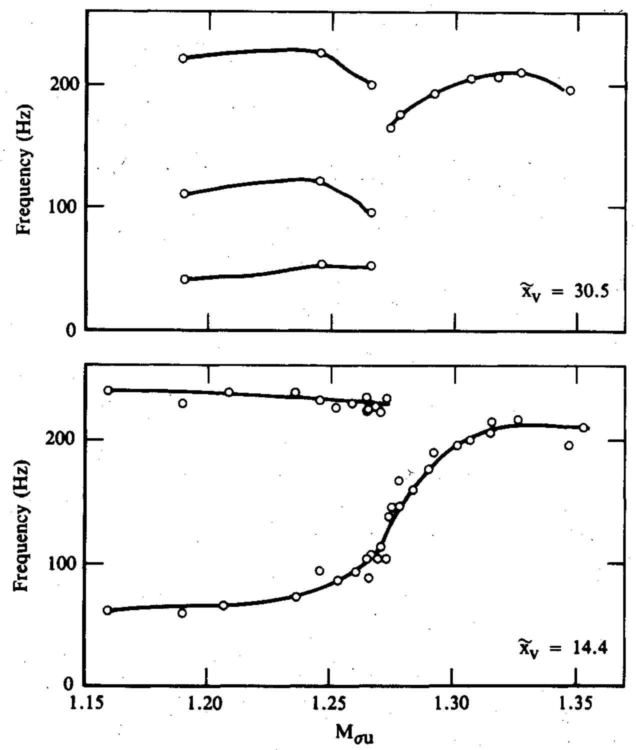

Fig. 10 Mach number dependence of shock motion spectral peaks for two diffuser lengths.

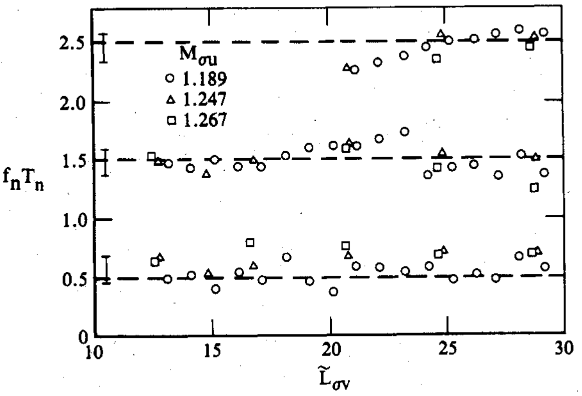

Fig. 11 Normalized natural frequencies for attached flow.

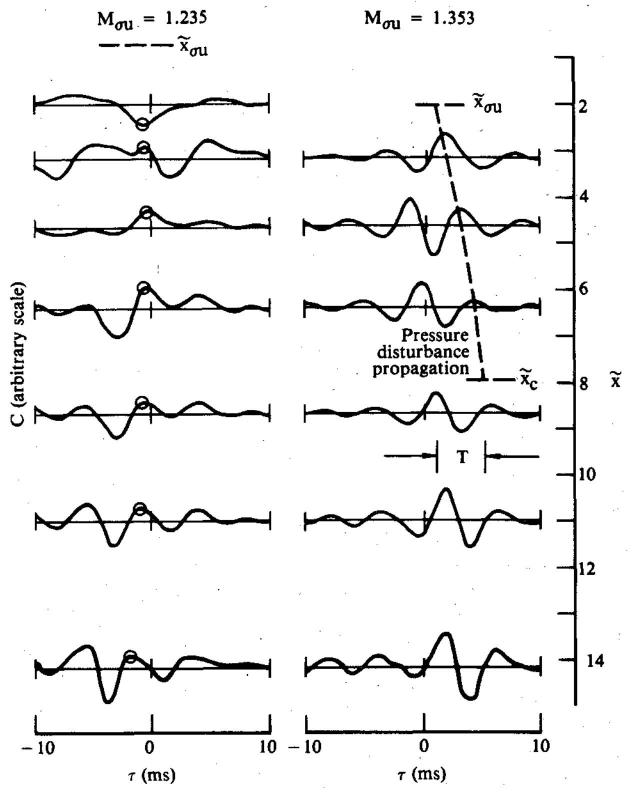

Fig. 12 Cross correlation of shock motion with top wall static pressures.

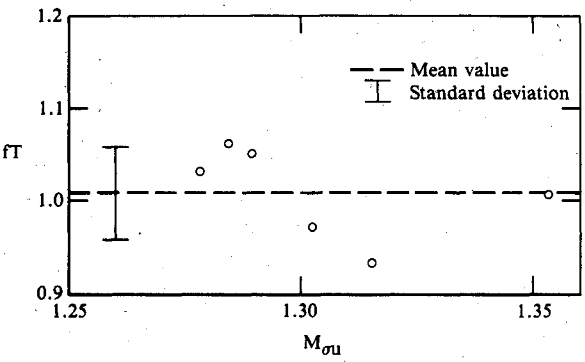

Fig. 13 Normalized natural frequencies for separated flow.

where ϕ is the (frequency-dependent) phase shift introduced by reflection from the shock. This leads to a transcendental equation for f_n. A convenient normalization of f_n is obtained using the time T_n taken by the nth acoustic mode to propagate from the channel end to the shock and back,

$$T_n = 2\int_{x_\sigma}^{x_v} \frac{dx}{a(x)\,[1 - M^2(x)]} + \frac{\phi_n}{2\pi f_n} \tag{4}$$

Introducing T_n into Eq. (3) yields

$$f_n T_n = (2n-1)/2 \tag{5}$$

which is cast in the standard form for an open/closed organ pipe. T_n was determined from Eq. (4) using the core total and wall static pressures, the plenum total temperature, and Culick's theory[19] for ϕ based on the measured natural frequencies. Figure 11 shows the natural frequencies normalized according to Eq. (5). The agreement is excellent, suggesting that longitudinal acoustic oscillations are indeed the mechanisms accounting for the observed spectral peaks and that Eq. (3) yields good estimates for engineering purposes.

Figure 12 contains the cross correlation between the unsteady shock displacement, $x_{\sigma m}(t)$, and the unsteady top wall pressures, $p_{su}(x,t)$, for both attached and separated flow conditions in the unextended channel. The signals were low-pass filtered at 500 Hz before processing to remove the contributions from boundary-layer turbulence in the pressure data.

The interaction between counterpropagating acoustic waves of equal frequency in the presence of a mean flow yields an envelope function modulating a propagating wave (see Appendix). The envelope function dictates the location of nodal points. The phase velocity of the propagating wave depends on the mean flow velocity and reaches a limit of infinity for a fluid at rest (a true standing wave).

The cross correlation for the weak shock ($M_{\sigma u} = 1.235$) near the shock is complicated by the presence of two time scales, related to the two natural frequencies. Only the higher frequency mode appears downstream; the fundamental mode approaches a node at the exhaust. Close inspection of the single-mode patterns reveals the presence of the upstream-traveling wave. The phase velocities determined from the time differences between successive circled peaks agree well with calculations based on Eq. (A2).

The presence of a node in the second harmonic is also clear from the circled extrema. The extrema change sign between the first and second measuring stations because of the 180 deg phase shift as the node is crossed. The location of the mth node x_m for the nth harmonic in a channel with mean flow and a phase shift ϕ at the upstream end is given by the integral equation,

$$\int_{x_\sigma}^{x_m} \frac{\mathrm{d}x}{a(x)\,[1-M^2(x)]} = \frac{1}{4f_n}\left(2m-1-\frac{\phi}{\pi}\right), \quad m=1,2,\ldots,n \tag{6}$$

For the present case, the calculation places the ($n=2$, $m=1$) node at $\tilde{x}=2.54$, in general agreement with the location of the cross-correlation sign change.

Not all higher modes are present in the shock motion spectra. There are no significant contributions above 250 Hz, the cutoff frequency of the shock response characteristics. Up to $L_{\sigma v} \cong 20$, this frequency range includes the first two modes. For longer channels, the frequency f_3 falls below 250 Hz, and the corresponding peak appears in the shock spectrum (Fig. 11).

Strong Shock

Shock displacement PSDs for the SIS mode invariably possess a single peak at a relatively high frequency (170-250 Hz), similar to that in Fig. 9 (bottom). The corresponding natural frequencies are independent of the channel length $L_{\sigma v}$, indicating that the natural frequencies cannot be attributed directly to longitudinal acoustic modes involving the entire channel length. The mechanism is not clear; however, observations allow at least two possible explanations.

One possibility is that the spectral peak is determined jointly by the shock response characteristics and the pressure spectrum in the vicinity of the cutoff frequency; the declining sensitivity and increasing spectral content produce a peak. If this is the case, then the local rate of the area change at the shock would be an important parameter in determining the shock frequency. If the pressure PSD possesses no significant peaks near or below the cutoff, then this mechanism could explain both the independence of natural frequency from $L_{\sigma v}$ and the absence of higher harmonics.

The second possibility is that the frequencies are governed by a characteristic length scale that is significantly smaller than, and independent of, the duct length. These criteria are satisfied by the core flow length $L_{\sigma c}$, which decreases rapidly at separation (Fig. 5) and is not affected by the addition of extra channel length segments.

The natural frequencies in the SIS range vary linearly with $1/L_{\sigma c}$ but do not follow Eq. (3) even if x_v is replaced by x_c. This result suggests that the oscillations are not simple longitudinal acoustic modes associated with the core flow region acting as a cavity.

Convective effects associated with the top wall boundary layer are reflected by the cross correlations between the unsteady shock and top wall pressures for separated flow (Fig. 12), which show a downstream movement of pressure disturbances. The time T needed by a particular feature of the cross correlation (such as an extremum) to move from the shock to the end of the core flow can be determined easily. This process is repeated for data corresponding to other Mach numbers to evaluate the product fT (Fig. 13). The fT values are in the range 1 ± 0.06, which compares with a 38% variation of the natural frequencies. This collapse of the data, accomplished by the normalization using T, strongly suggests that the boundary layers participate significantly in the oscillations.

The importance of boundary-layer-convected perturbations in strong shock flows is supported by detailed, time-dependent velocity field measurements.[15] It appears likely that strong shock oscillations are sustained by a feedback loop consisting of upstream-propagating acoustic waves and downstream-convected perturbations in the boundary layers. The acoustic waves perturb the shock, which then modulates the properties of the boundary layer emerging from the interaction region and thereby initiates the downstream-moving portion of the cycle. This type of mechanism is predicated on the presence of boundary layers, which exist only where the core flow is present; beyond the merger, the wall layers disappear as separate entities and begin a gradual transition toward fully developed channel flow. It is thus not unreasonable to find that the length of the core flow is an important determinant of the natural oscillation frequency.

Summary

The investigated diffuser displayed attached flows below a shock Mach number of 1.27 and shock-induced separation above 1.28, with intermittent transition between these limits. Broadband pressure and narrowband shock displacement oscillations occurred at all conditions at relatively small amplitudes compared with results from earlier experiments with larger area-ratio diffusers.

For attached flow, the natural frequencies in the unsteady shock motion scale inversely with the shock-to-exhaust distance, and the mechanism of the oscillation is the propagation of acoustic waves along the channel in both directions. Modes up to the third harmonic are observed. The frequencies of these oscillations are well predicted by inviscid, one-dimensional, linearized (acoustic) calculations.

In the case of shock-induced separation, both pressure and shock displacement amplitudes are greater than those for attached flow, and the single natural frequency observed is independent of duct length and not predicted by acoustic theory. The mechanism of this mode of oscillation is not clear. The frequency appears to scale with the length of the inviscid core flow and is related to convective effects in the boundary layer. The observations, however, also allow another explanation that links the natural frequency to the low-pass filter-like response of the terminal shock as it reacts to the broadband pressure fluctuation environment created by the highly turbulent, separated boundary layers.

Appendix

Consider a channel containing a nondispersive, uniform fluid moving at constant velocity u with acoustic waves of unit amplitude and equal frequency traveling up- and downstream. The mean fluid motion is described by replacing k with $k/(1 \pm M)$ since the rest-frame frequency is constant $[\omega = ka = k_+(a+u) = k_-(a-u)]$. Assume that the downstream wave lags behind the upstream wave at $x=0$ by a phase angle of ϕ. The sum of the two acoustic waves,

$$\cos\left(\frac{kx}{1-M}+\omega t\right)+\cos\left(\frac{kx}{1+M}-\omega t+\phi\right) \tag{A1}$$

can also be written as the product

$$2\cos\left(\frac{kx}{1-M^2}+\frac{\phi}{2}\right)\cos\left(\frac{kMx}{1-M^2}+\omega t-\frac{\phi}{2}\right) \tag{A2}$$

The first factor is a function of x only and can be interpreted as an envelope for oscillations similar to those in the conventional standing-wave pattern with no flow. The second factor represents an upstream-traveling wave that is modified by the envelope.

The characteristic frequencies for a channel of length L can be determined by imposing the appropriate boundary conditions. Assume the channel open at $x=L$, corresponding to a pressure node. At the upstream end, we have already imposed a phase delay of ϕ and tacitly assumed the reflection coefficient to be unity by specifying the two waves to be of equal amplitude. The characteristic frequencies then become, in normalized form,

$$\frac{f_n L}{a} = \left(2n - 1 - \frac{\phi}{\pi}\right)\left(\frac{1-M^2}{4}\right), \quad n=1,2,3,\ldots \qquad \text{(A3)}$$

The location of the mth nodal point for the nth mode is given by

$$\frac{x_m}{L} = \frac{(2m-1)\pi - \phi}{(2n-1)\pi - \phi}, \quad m=1,2,\ldots,n \qquad \text{(A4)}$$

When the velocity of the fluid and the speed of sound vary along the channel, the characteristic frequencies can be calculated through the following heuristic argument: at any given time, the spatial distribution of the wave, i.e., the phase difference between any point x and the origin, can be determined by calculating the time the wave takes to travel from $x=0$ to x, divided by the period of the oscillation, T $(=1/f)$. The phase is given by

$$2\pi\frac{t}{T} = \frac{2\pi}{T}\int_0^x \frac{\mathrm{d}x'}{a(x')+u(x')} = \int_0^x \frac{\omega \mathrm{d}x'}{a(x')+u(x')}$$
$$= \int_0^x \frac{k(x')}{1+M(x')}\mathrm{d}x' \qquad \text{(A5)}$$

Replacing the spatial terms in Eq. (A1) with the appropriate integrals and applying the appropriate boundary conditions will yield the solutions (given in the text) for cases where a and u are functions of x.

The above idealized derivation yields the same results as a generalized derivation involving more realistic boundary conditions.[20]

Acknowledgments

This work was sponsored in part by Air Force Office of Scientific Research Contract F49620-77-C-0082 and in part by the McDonnell Douglas Independent Research and Development program.

References

[1] Sajben, M., Kroutil, J. C., and Chen, C. P., "A High-Speed Schlieren Investigation of Diffuser Flows with Dynamic Distortion," AIAA Paper 77-875, 1977.

[2] Sajben, M., Kroutil, J. C., and Chen, C. P., "Unsteady Transonic Flow in a Two-Dimensional Diffuser," *Unsteady Aerodynamics,* AGARD Conference Proceedings No. 227, 1977, pp. 13-1 to 13-14.

[3] Chen, C. P., Sajben, M., and Kroutil, J. C., "Shock-Wave Oscillations in a Transonic Diffuser Flow," *AIAA Journal,* Vol. 17, Oct. 1979, pp. 1076-1083.

[4] Sajben, M. and Kroutil, J. C., "Effects of Initial Boundary-Layer Thickness on Transonic Diffuser Flows," *AIAA Journal,* Vol. 19, Nov. 1981, pp. 1386-1393.

[5] Liou, M.-S., "Analysis of Viscous-Inviscid Interactions in Transonic Internal Flows with a Shock Wave and Mass Transfer," AIAA Paper 81-0004, 1981.

[6] Liou, M.-S., Coakley, T. J., and Bergmann, M. Y., "Numerical Simulation of Transonic Flows in Diffusers," AIAA Paper 81-1240, 1981.

[7] Knight, D. D., "Improved Calculations of High Speed Inlet Flows, Part I: Numerical Algorithm," *AIAA Journal,* Vol. 19, Jan. 1981, pp. 34-41.

[8] Knight, D. D., "Improved Calculation of High Speed Inlet Flows, Part II: Results," *AIAA Journal,* Vol. 19, Feb. 1981, pp. 172-179.

[9] Gadd, G. E., "Interaction Between Normal Shock Waves and Turbulent Boundary Layers," ARC 22559, R&M 3252, 1952.

[10] Pearcey, H. H., "Shock-Induced Separation and Its Prevention by Design and Boundary Layer Control," *Boundary Layer and Flow Control,* Vol. 2, edited by G. V. Lachmann, Pergamon Press, New York, 1961.

[11] Kerrebrock, J. L., "Flow in Transonic Compressors," *AIAA Journal,* Vol. 19, Jan. 1981, pp. 4-19.

[12] Rogers, T., "Ramjet Inlet/Combustor Pulsation Study," Naval Weapons Center, Rept. NWC TP 6053, Jan. 1980.

[13] Roos, F. W., "Fluid Mechanics Related to Airfoil Buffeting: A Review," McDonnell Douglas Corp., Rept. MDC Q0456, Dec. 1971.

[14] Sajben, M., Bogar, T. J., and Kroutil, J. C., "Forced Oscillation Experiments in Supercritical Diffuser Flows with Application to Ramjet Instabilities," AIAA Paper 81-1487, 1981; *AIAA Journal* (to be published).

[15] Salmon, J. T., Bogar, T. J., and Saljben, M., "Laser Velocimeter Measurements in Unsteady, Separated, Transonic Diffuser Flows," AIAA Paper 81-1197, 1981; *AIAA Journal* (to be published).

[16] Sajben, M. and Crites, R. C., "Real-Time Optical Measurement of Time-Dependent Shock Position," *AIAA Journal,* Vol. 17, Aug. 1979, pp. 910-912.

[17] Roos, F. W. and Bogar, T. J., "Direct Comparison of Hot-Film Probe and Optical Techniques for Sensing Shock-Wave Motion," AIAA Paper 81-0157, 1981.

[18] Bower, W. W., "Analytical Procedure for the Calculation of Attached and Separated Subsonic Diffuser Flows," *Journal of Aircraft,* Vol. 13, Jan. 1976, pp. 49-56.

[19] Culick, F. E. C., "The Response of Normal Shocks in Inlet Diffusers," AIAA Paper 81-1431, 1981.

[20] Sajben, M. and Bogar, T. J., "Unsteady Transonic Flow in a Two-Dimensional Diffuser: Interpretation of Results," McDonnell Douglas Corp., Rept. MDC Q0779, March 1982.